ADVANCED FUNCTIONAL MATERIALS

FULL PAPER

DOI: 10.1002/adfm.200700139

Structure–Property–Function Relationships in Nanoscale Oxide Sensors: A Case Study Based on Zinc Oxide**

By *Sebastian Polarz*,* *Abhijit Roy*, *Michael Lehmann*, *Matthias Driess*, *Frank Einar Kruis*,* *Andreas Hoffmann*, and *Patrick Zimmer*

Chemical sensing on oxide sensors is a complex phenomenon involving catalytic activity as well as electronic properties. Thus, the properties of oxide sensors are highly sensitive towards structural changes. Effects like surface area, grain size, and, in addition, the occurrence of defects give separate contributions to the current. Structure–property–function relationships can be elucidated using a combination of state-of-the-art analytical techniques. It is shown, that impurity atoms in the oxide lattice influence the performance of ZnO sensors more strongly than the other factors.

1. Introduction

Transition metal oxides exhibit an amazing spectrum of properties and applications.[1,2] ZnO is an excellent example as it possesses interesting piezoelectric and electromechanical coupling properties, and it has been used in UV light-emitting diodes, lasers, photovoltaic solar cells, UV-photodetectors, varistors, and even heterogeneous catalysis.[3–15] For the current manuscript, the combination of semiconducting properties and catalytic surface activity is most relevant: the electrical resistance of ZnO changes depending on the amount of surface-bound oxygen atoms.[16] Interestingly, ZnO was one of the first materials to be explored for chemical sensing.[17] However, to date most of the attention in the field of metal-oxide sensors was devoted to SnO_2,[18,19] and not ZnO sensors,[20–25] presumably because the latter devices suffered from insufficient long-term stability.[18] It is already well established for metal-oxide sensors that the sensitivity depends on various factors that can be summarized as textural parameters: low-area intergrain and interagglomerate contacts, lower film thickness, and high porosities of the sensor matrix are beneficial for performance.[26,27] Consequently, a considerable amount of effort has been made to achieve a highly sensitive gas sensor by engineering the above-mentioned texture parameters. However, the intrinsic properties of semiconducting oxides are determined by more than morphological factors. Therefore, efforts to understand the contribution of nontexture factors (local or nonlocal deviations in chemical composition as well as microstructural defects) regarding the performance of chemical sensors are of enormous importance.[28]

2. Results and Discussion

2.1. Sensor Preparation

We became interested in this subject because of the limited performance of current ZnO sensors and because we reported recently the synthesis of various ZnO materials from special organometallic precursors.[15,29–34] It is important to note that the volatility of alkyl–Zn–alkoxide precursors allows the preparation of metal-oxide nanoparticles in the gas phase using the so-called chemical vapor synthesis (CVS) process, as we demonstrated recently (see Fig. 1a).[31,33,34] The latter results are the basis for the work presented here. Because quite high temperatures are applied in CVS but nanoscale particles are still obtained, the idea was that this would allow the preparation of stable but still very active ZnO sensors. The experimental procedure for the sensor-device preparation is schematically depicted in Figure 1 and described in the Experimental section. The aerosol-containing ZnO particles were deposited on a sensor grid as shown in Figure 1b.

2.2. Sensor Performance

In order to oxidize the organic shell of the precursor, different amounts of oxygen were added to the precursor aerosol

[*] Prof. S. Polarz
University of Konstanz, Department of Chemistry
78457 Konstanz (Germany)
E-mail: sebastian.polarz@uni-konstanz.de
Dr. F. E. Kruis, Dr. A. Roy
Department of Electrical Engineering and Information Technology
University of Duisburg–Essen
47057 Duisburg (Germany)
E-mail: einar.kruis@uni-due.de
Prof. M. Lehmann, Prof. M. Driess, Dr. A. Hoffmann, P. Zimmer
Department for Mathematics and Natural Sciences
Straße des 17. Juni 135, 10623 Berlin (Germany)

[**] We thank the Deutsche Forschungsgemeinschaft (Emmy-Noether scholarship, SPP 1119) for financial support. Dr. E. Bill and Prof. K. Wieghardt are gratefully acknowledged for measuring EPR spectra. The possibility and support for using the spherical-aberration-corrected FEI Tecnai F20 transmission electron microscope in the workgroup of Prof. Hannes Lichte at the Triebenberg Lab of the TU Dresden is gratefully acknowledged. Supporting Information is available online from Wiley InterScience or from the author.

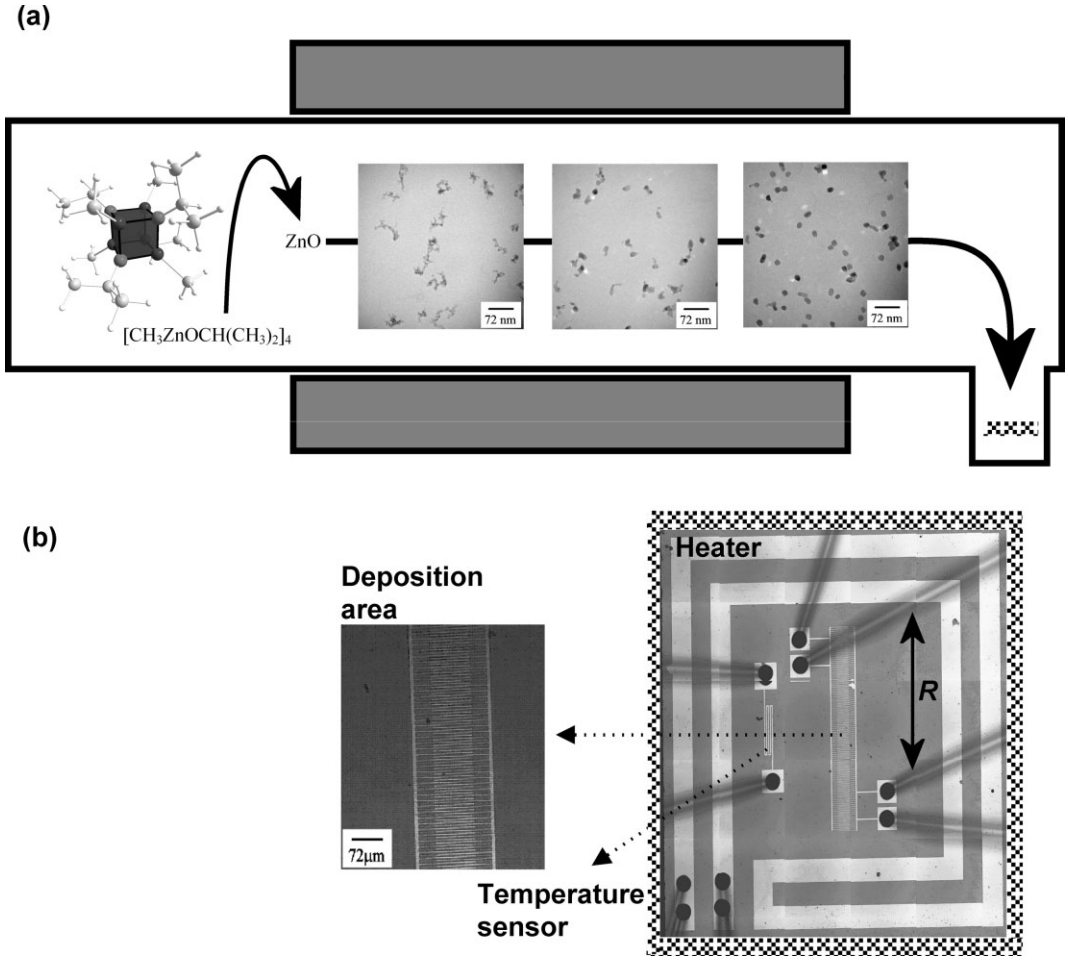

Figure 1. a) The stepwise formation of ZnO nanoparticles from the molecular source $[CH_3ZnOCH(CH_3)_2]_4$ in the gas phase: the precursor aerosol is injected into a tube furnace. Formation of ZnO clusters occurs, followed by sintering and densification. The particles can be deposited on a sensor array (gray rectangle). The formation process of the ZnO in the gas phase is described in much more detail in a previous report from where the transmission electron microscopy images have also been reproduced [33]. b) Microscopic images of the sensor array indicating the positions where the ZnO nanoparticles have been deposited.

(0.2 % for ZnO^{I}, 2 % for ZnO^{II}, 20 % for ZnO^{III}); time–temperature histories were identical. The sensors were tested with ethanol (Fig. 2). The prepared materials showed measurable sensor activity even at very low partial pressures of the analyte ≤1 ppm ethanol (see Fig. 2a and Supporting Information, Fig. SI1; ppm = parts per million). The absolute numbers for the sensitivities are significantly higher than recently developed ZnO sensors.[23,24,35–40] Even in comparison to recent SnO_2 sensors (sensitivity $S \approx 1000$ at an ethanol partial pressure $p_{EtOH} = 500$ ppm; for a definition of the sensitivity see the Experimental section)[41] the ZnO sensors exhibit extraordinary performances ($S \approx 8000$ at $p_{EtOH} = 500$ ppm). Furthermore, the materials seem to have overcome the long-term instability problem that has been reported for many ZnO sensors.[18] Even after 200 days (see Fig. SI2, Supporting Information) the sensor device is characterized by constantly high sensitivity values. The advanced stability can be rationalized by the high temperatures used in the CVS process ($T = 1173$ K) in comparison to the operating temperature of the gas sensor ($T = 673$ K). Because the operating temperature is comparably low, further sintering of the ZnO particles is prohibited.

Interestingly, it was also seen that the oxygen partial pressure p_{ox} has a stronger impact than expected on the sensors (Fig. 2a). The sensitivities differ roughly by one order of magnitude. To express the differences in sensor performance seen in Figure 2a with only one value, the averaged, relative sensitivities (S_{rel}) were calculated by first normalizing the highest sensitivity to 1 for all partial pressures of ethanol, followed by arithmetic averaging (Fig. 2b). It is seen that ZnO^{I} prepared at the lowest p_{ox} possessed sensitivities about one order of magnitude higher than the ZnO^{III} sensor prepared for the highest p_{ox}, and that ZnO^{II} is in between. There is a clear correlation between p_{ox} and S_{rel}.

2.3. Texture Effects

Because chemical sensing is such a complex phenomenon, there are several possibilities to explain the observed differ-

ADVANCED FUNCTIONAL MATERIALS

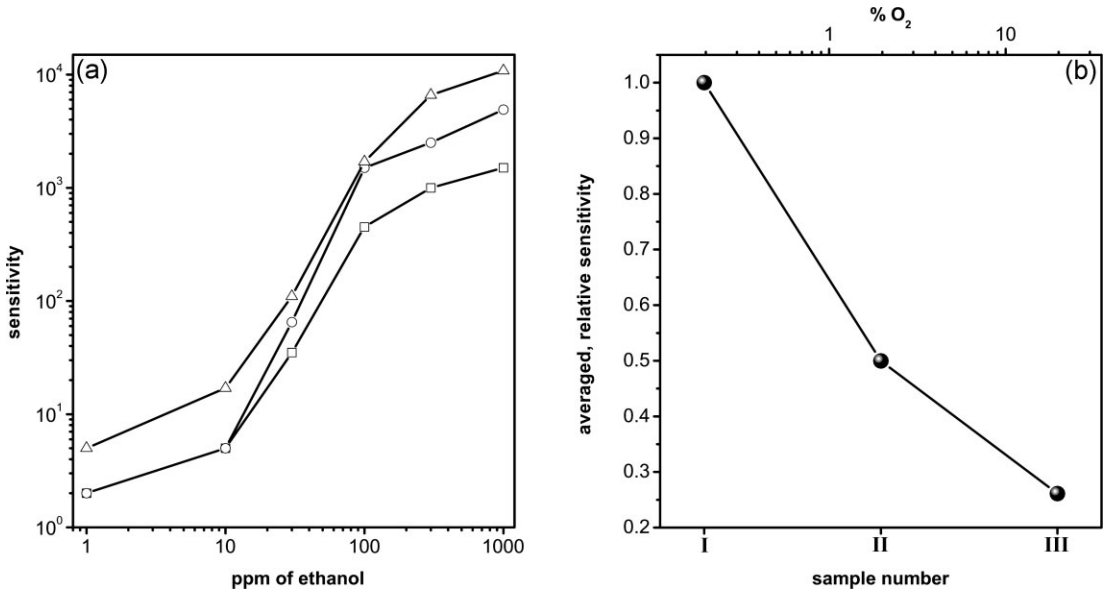

Figure 2. a) Sensitivity values for different ethanol partial pressures: ZnO^{I} material (triangles), ZnO^{II} material (circles), and ZnO^{III} material (squares). b) The averaged relative sensitivities for the samples in this study.

ences: Eventually, even at low p_{ox}, it may be suspected that products other than ZnO can be formed. However, this seems not to be the case, as powder X-ray diffraction (PXRD) recorded from $ZnO^{I–III}$ indicates (Fig. 3a). In all three cases only the reflections for ZnO are found, and there are hardly any differences. Also in transmission electron microscopy (TEM) images (Fig. 2b), the samples look very similar. TEM images of the deposited aerosols indicate that the ZnO materials are composed of crystalline, polydisperse particles with a size of $D_{p,TEM} \approx 7–15$ nm, although some larger particles are present as well (Fig. 2b). At this point, it is important to note that, generally, sensitivity increases nonlinearly when the D_p of the metal oxide approaches the thickness of the so-called space-charge layer.[16] Consequently, a more refined analysis of the ZnO microstructure is needed to see if the microstructure could explain the observed differences in S_{rel}.

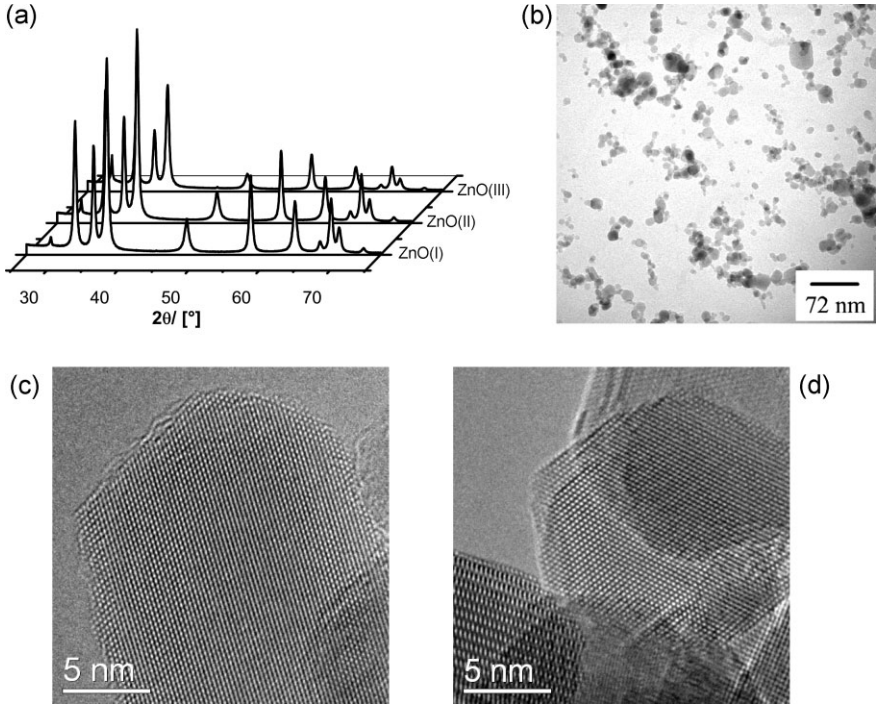

Figure 3. a) PXRD-patterns of the samples $ZnO^{I–III}$. b) TEM image of the ZnO^{III} sample. High-resolution TEM images of ZnO^{I} (c) and ZnO^{III} (d).

In order to extract more details about the microstructure from the PXRD data a Warren–Averbach (WA) analysis was performed (see Fig. SI3, Supporting Information). The results of the WA analysis are summarized in Table 1. It seems that, according to PXRD, the samples ZnO^{I} and ZnO^{III} are very similar to each other, whereas sample ZnO^{II} shows the strongest deviations. ZnO^{II} is characterized by the largest particles and the largest particle asymmetry (platelet morphology). Regarding microstrain and differences in lattice parameters, all three ZnO samples are very close to bulk ZnO, which is a first indication that the number of structural defects in these samples is not very large. Considering only the crystallite sizes, one would expect ZnO^{III} to exhibit the best sensor performance, closely followed by ZnO^{I}, with ZnO^{II} being the worst. Apparently this is not the case, meaning that the development of the crystallite sizes or other microstructural parameters

Table 1. Comparison of sensor performance to microstructure parameters.

	S_{rel}	$D_{p,PXRD}$ [nm]	Particle asymmetry along {101}	Microstrain [%]	Δa [Å]	Δc [Å]
ZnO^{I}	1	22.24	1.24	0.076	0	0.4
ZnO^{II}	0.499	27.01	1.53	0.129	0.74	1.52
ZnO^{III}	0.261	22.02	1.35	0.09	0.66	1.51

(Table 1) cannot explain the differences in sensitivities for the different samples either. It is not absolutely correct to consider only the grain size, because in the case of strong agglomeration, the particle size relevant for the space-charge layer can be different from the grain size. Therefore, particle sizes of the actual porous, spongelike ZnO sensor material (Fig. 4a) were estimated independently on the basis of surface-area data ($D_{p,vol}$), assuming that the particle morphology is almost spherical (Fig. 3b–d).

N_2 isotherms were recorded (Fig. 4b) and values for $D_{p,vol}$ of the order of 20 nm were calculated for all three ZnO samples. $D_{p,vol}$ is in general slightly larger than the real D_p because of necking between the ZnO particles in the sensor material. Because $D_{p,vol}$, $D_{p,PXRD}$, and $D_{p,TEM}$ are quite close to each other, the assumption that the particle size one has to consider for the sensors is equal to the primary grain size is sufficiently supported. However, what leads to the observed sensing differences is still unanswered.

A second look at the isotherms (Fig. 4b) reveals that the samples possess different surface areas. It is known from the literature that the sensor performance is generally very sensitive to the total surface area. The isotherms show a N_2 uptake at higher relative pressures indicating a significant amount of large pores. Calculation of the Brunauer–Emmett–Teller (BET) surface area reveals that for lower oxygen partial pressures in the CVS, ZnO materials with lower surface area are obtained (Fig. 4c). It is obvious that the trend regarding the surface areas is opposite to the expected surface-dependency of the sensitivities: higher sensitivities are achieved for smaller surface areas. It can be concluded that the surfaces of ZnO^{I} are inherently more active as a sensor. This means that an effect which is stronger than the accessible surface area or other texture factors determines the properties of the ZnO sensors. Summarizing the first part of the manuscript it can be said that, for ZnO, texture effects may have some impact on the sensor performance, but none of them explains the correlation introduced in Figure 2.

2.4. Nontexture Effects

At this point, it makes sense to investigate nontexture effects as well. Likely candidates for catalytically more active surfaces

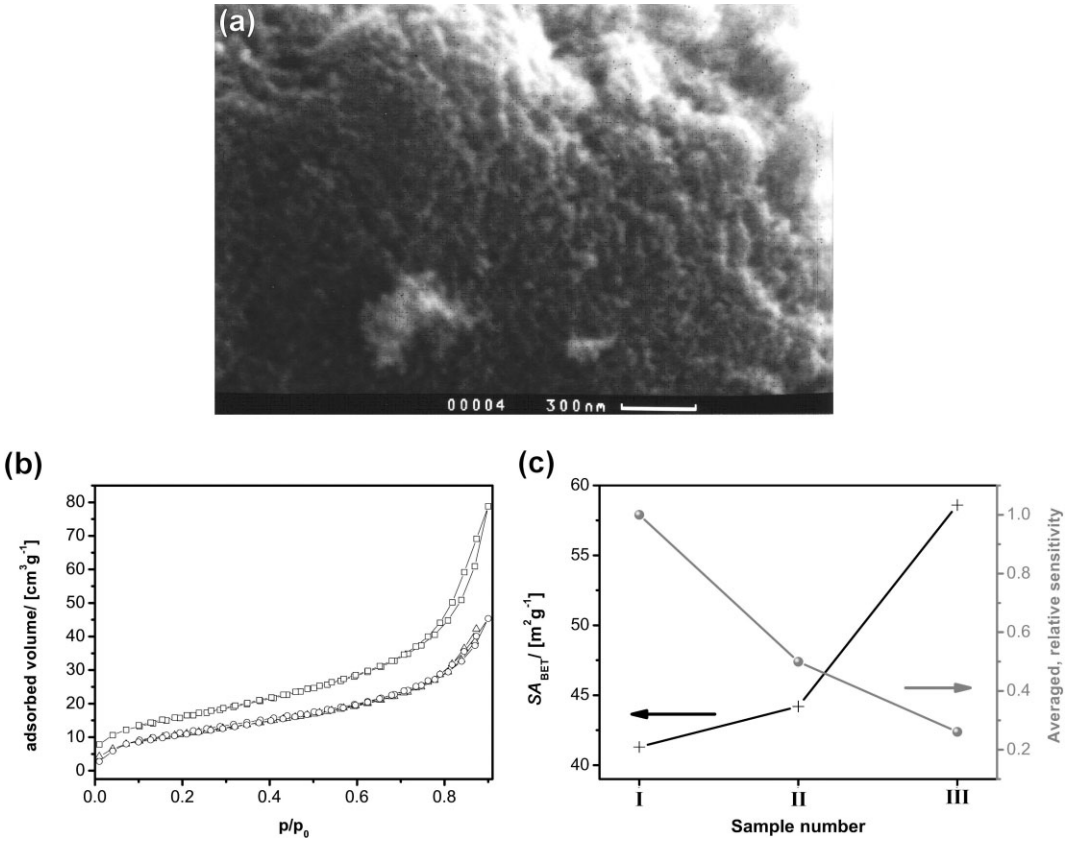

Figure 4. a) Scanning electron microscopy image of a representative ZnO sample, b) N_2-physisorption isotherms (ZnO^{I} (triangles), ZnO^{II} (circles), and ZnO^{III} (squares), and c) Brunauer–Emmett–Teller (BET) surface areas (SA_{BET}) of the ZnO^{I-III} samples (black line).

are ZnO materials containing oxygen vacancies, as described recently.[29,32] It was reported that the occurrence of oxygen vacancy sites can be traced via trapped electrons detectable by electron paramagnetic resonance (EPR) spectroscopy.[32] An EPR signal with a *g*-factor value of ca. 2.0 is characteristic of a single electron trapped on an oxygen-vacancy site, whereas signals with a *g*-factor of ca. 1.96 are indicative of impurity atoms (Zn, C, and others) on interstitial sites in the ZnO lattice.[29,32] EPR spectra of all three ZnO samples were measured under identical conditions and care was taken that the same sample volume and mass were used. This allows a semiquantitative comparison of the EPR spectra with each other. Only one EPR signal at a *g*-factor of 1.96 was found for all three $ZnO^{I–III}$ samples, meaning that the samples do not contain oxygen vacancies. This result is not what we had initially expected because we had hoped to obtain samples containing more oxygen vacancies when less oxygen was used in the synthesis gas. However, on a second glance the latter result is not so unusual. In previous investigations we were able to show that ZnO with high amounts of oxygen vacancies can only be accessed using a kinetic preparation route,[32] whereas the CVS process is predominantly thermodynamically controlled.[33] This fits with the observation made by others that oxygen vacancies are not thermodynamically stable at ambient conditions,[42] but are only represented in kinetically stabilized states.

The signal at g-factor values of ca. 1.96 could originate from various shallow donor centers in the ZnO lattice.[32,43–45] In the case presented here, only two alternatives for potential shallow donors have to be considered: interstitial Zn atoms and C atoms coordinated by oxygen in the carbonate mode.[32] Because the amount of the impurity atoms is expected to be in the ppm range, it is very difficult to track them by using elemental-analysis methods or crystallographic methods. However, because the intensity of the signal at a *g*-factor of 1.96 is weaker for $ZnO^{I/II}$ than for ZnO^{III} (Fig. 5b), it is rather unreasonable to suggest the formation of more interstitial Zn atoms if p_{ox} is increased. It appears much more likely that the signal at a *g*factor of 1.96 is caused by entrapped C atoms in the ZnO lattice originating from the precursor. Chemically, the probability of entrapment rises if the oxygen partial pressure is increased, because the oxidation of the organic shell of the molecular precursor (Fig. 1) facilitates the formation of CO_2, which at the high temperatures used for the CVS process (see the Experimental section) can react to form carbonate

$$[CH_3ZnOCH(CH_3)_2]_4 + 19\,O_2 \rightarrow 4\,ZnO + 12\,CO_2 + 14\,H_2O$$

$$4\,ZnO + CO_2 \rightarrow 3\,ZnO \cdot ZnCO_3$$

On the other hand, if the amount of oxygen is limited, the elimination of organic leaving groups from the heterocubane framework is favored

$$[CH_3ZnOCH(CH_3)_2]_4 \rightarrow 4\,ZnO + CH_3CH{=}CH_2 + CH_4$$

The amount of entrapped shallow donors seems to be quite relevant for the sensor performance of ZnO as can be concluded from Figure 5b. For the first time, a reasonable correlation between one feature of the real structure of the ZnO materials and S_{rel} is identified: the smaller the amount of shallow donors, the better S_{rel} is. In order to support this hypothesis, an additional analytical measure for the presence of carbonate species would be very valuable. Carbonate groups should be easily detectable even in small amounts by IR spectroscopy. Therefore, IR spectra of the samples $ZnO^{I–III}$ were measured (Fig. SI4, Supporting Information). The IR spectra of the ZnO samples are characterized by an intense band at 500 cm^{-1} (the Zn–O vibration) and a number of low intensity bands in the fingerprint region characteristic for carbonates (1625 cm^{-1}). It is possible to compare the different Fourier transform IR (FTIR) measurements with each other if the spectra are referenced internally to the intensity of the Zn–O band. Then, it becomes evident that the IR spectra support the trend proposed from the EPR results. The oxygen partial pressure used for the CVS influences the formation of the carbonates.

A new question emerges: Is the variation of the sensor properties a real nontexture effect or does surface coverage of the ZnO particles with carbonate influence the sensors negatively? In order to answer this question, high-resolution TEM (HRTEM) data was acquired; it is shown in Figure 3c and d. The HRTEM data are in good agreement with PXRD. One finds polydisperse highly crystalline particles with a significant

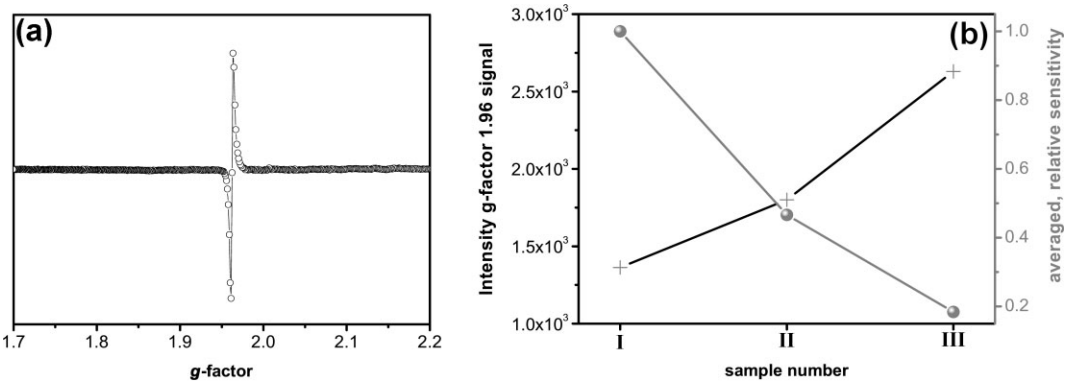

Figure 5. Representative EPR spectrum (measured on the ZnO^{III} sample) at 298 K (a) and comparison of S_{rel} and the intensity of the EPR signal at a *g*-factor of 1.96 for the samples $ZnO^{I–III}$.

fraction of particles in the 10–15 nm range. It is important to note that the special HRTEM method used allows reliable imaging of nanoparticle surfaces.[46–49] It can be seen from the HRTEM images that the surfaces of the nanoparticles are very clean, especially for the ZnO^{III} sample (Fig. 3d), which was characterized by the lowest sensitivities. Surface passivation by carbonate obviously cannot be the deciding factor. Considering all the results mentioned together, there are substantial indications that impurity atoms in the ZnO lattice affect the sensor properties of ZnO very strongly, potentially more than surface effects. Nevertheless, it is yet not clear how these impurity atoms influence the sensor. In order to elucidate this issue, UV–vis spectra in diffuse reflectance mode were recorded from all samples. Exemplarily, the spectrum of ZnO^{III} is shown in Figure 6a in comparison to bulk ZnO as a reference. It is seen that the band edge is shifted to lower energies accompanied by band tailing in the lower-energy region (Fig. 6a). The UV–vis data are supported nicely by photoluminescence (PL) measurements (Fig. SI5, Supporting Information). The maximum of the band-edge PL of sample ZnO^{III} is shifted to 3.12 eV and is significantly broadened in the low-energy region of the spectrum. Both factors, red-shift and band-tailing, will affect the surface-energy states of the ZnO particles in such a way that the tailing of the conduction band forming the space-charge layer is reduced (Fig. 6b). This, in turn, reduces the space-charge layer and leads to a decrease of surface reaction effects on the electrical properties of the system, finally decreasing the sensitivities.

3. Conclusions

New and highly active chemical sensors have been presented that overcome the lack of lifetime reported for previous ZnO sensors. Our results show that like for heterogeneous catalysts, the sensor properties depend significantly on the synthesis conditions. Texture effects (particle size and surface area) were balanced with nontexture effects (shallow-donor dopants), and it was seen that, unexpectedly, the latter are as important or even more important than texture effects. Chemical sensors are even more complex than thought.

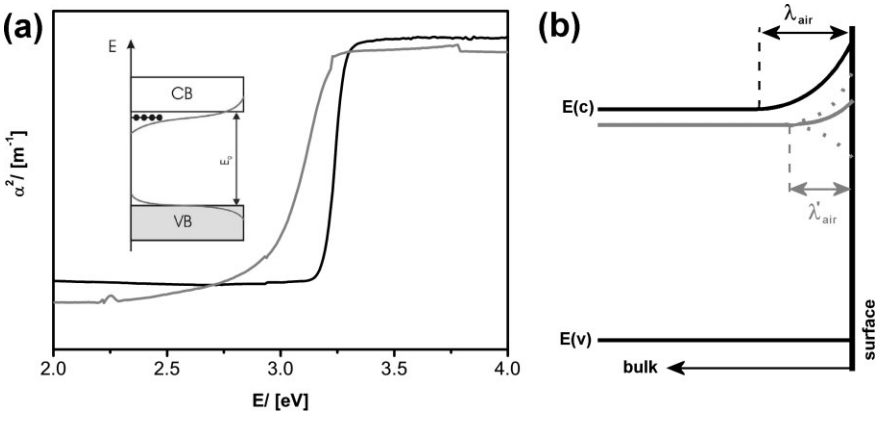

Figure 6. a) UV–vis spectra of ZnO^{III} with bulk ZnO as a reference. The inset shows how impurity atoms lead to band tailing and shift the band-edge to lower energies. b) A schematic representation of how impurity atoms may influence the space-charge layer with $E(v)$ = valence-band energy, $E(c)$ = conduction-band energy, and λ_{air} = space-charge layer. The gray color indicates that the ZnO is "doped" with impurity atoms.

4. Experimental

ZnO materials were prepared using the CVS technique as described previously [33]. The synthesis was carried out in a decomposition furnace under different oxygen concentrations: 0.2 %, 2 %, and 20 % (by volume). The temperature of the decomposition furnace was fixed at 1173 K and the residence time of the aerosol inside the decomposition furnace was ca. 2.5 s in all the experiments. The polydisperse aerosol of ZnO nanoparticles were directly deposited on the substrate with interdigitated Au electrodes (see Fig. 1) using an electrostatic precipitator operating under low pressure [50]. The thickness of the porous ZnO matrix was close to 15 μm for all three samples. Prior to gas-sensing measurements, the as-deposited ZnO nanoparticle films were annealed at 673 K for 24 h under ambient laboratory conditions. After annealing all the ZnO nanoparticle porous films show linear current–voltage characteristic under 1000 ppm of ethanol at all the temperatures between 298 K and 673 K, which clearly indicates the absence of any Schottky junction between the electrode and the particle films. The resistance measurements of the nanoparticle films under different gas environments were carried out using a fully automated gas-sensing setup as reported previously [51]. The gas-flow system allows control of the gas concentration between 1 and 1000 ppm (volume based) of the measured gas (ethanol in the present study) in dry synthetic air (20 % oxygen, 80 % nitrogen). The sensitivity (S) in the present study was determined by the ratio of the stable resistance of the ZnO in dry synthetic air (R_a) and the stable resistance in a reducing atmosphere (R_g): $S = R_a/R_g$. Each measurement was repeated at least three times.

The HRTEM images were recorded at the FEI Tecnai F20/Cs-corr transmission electron microscope located at the Triebenberg Lab of the TU Dresden. This microscope is equipped with a field-emission electron source and operates at 200 kV acceleration voltage. The spherical aberration of the objective lens is corrected by means of a Cs corrector, which allows the correction of all coherent aberrations up to the third order. As a consequence, surfaces of clusters are imaged without delocalization, showing the true positions of atomic columns. The TEM samples were prepared by shortly dipping a carrier covered with a holy C foil (Plano company, S147) in the solution, where the ZnO particles were dissolved in acetone. X-ray diffraction images were recorded with a Bruker–AXS D8 Advance using Cu Kα-radiation (wavelength $\lambda = 1.5418$ Å) and a position-sensitive-detector (PSD) diffractometer using Cu Kα radiation in the angular 2θ range from 25° to 85° with 0.015° steps. FTIR spectra were taken with a Bruker Vector 22 spectrometer (KBr-pellets). UV-vis spectra were recorded using a Perkin Elmer Lambda 20 spectrometer equipped with a reflecting sphere, Labsphere RSA-PE-20. Conventional transmission electron microscopy (CTEM) was performed on a Philips CM12 microscope (LaB_6 filament, 120 kV, Twin lens) equipped with an energy-dispersive X-ray spectrometer (EDX, type Oxford Link). X-band EPR spectra were recorded with a Bruker Elexsys E500 EPR spectrometer with an ER077R magnet (75 mm pole–cap distance), and an ER047 XG-T microwave bridge. N_2 physisorption was measured using a Micromeritics Gemini instrument.

Received: November 8, 2006
Revised: February 1, 2007
Published online: ■

[1] B. Raveau, *J. Eur. Ceram. Soc.* **2005**, *25*, 1965.
[2] C. N. R. Rao, J. Gopalakrishnan, *Acc. Chem. Res.* **1987**, *20*, 228.
[3] D. C. Look, *Mater. Sci. Eng. B* **2001**, *80*, 383.
[4] C. Hickerne, *IEEE Trans. Microwave Theory Tech.* **1969**, *MT17*, 957.
[5] D. C. Look, B. Claftin, *Phys. Status Solidi B* **2004**, *241*, 624.
[6] B. K. Meyer, H. Alves, D. M. Hofmann, W. Kriegseis, D. Forster, F. Bertram, J. Christen, A. Hoffmann, M. Strassburg, M. Dworzak, U. Haboeck, A. V. Rodina, *Phys. Status Solidi B* **2004**, *241*, 231.
[7] M. A. Martinez, J. Herrero, M. T. Gutierrez, *Sol. Energy Mater. Sol. Cells* **1997**, *45*, 75.
[8] N. A. Anderson, X. Ai, T. Q. Lian, *J. Phys. Chem. B* **2003**, *107*, 14414.
[9] K. Keis, J. Lindgren, S. E. Lindquist, A. Hagfeldt, *Langmuir* **2000**, *16*, 4688.
[10] E. Monroy, F. Omnes, F. Calle, *Semicond. Sci. Technol.* **2003**, *18*, R33.
[11] D. R. Clarke, *J. Am. Ceram. Soc.* **1999**, *82*, 485.
[12] H. H. Kung, *Catal. Rev. Sci. Eng.* **1980**, *22*, 235.
[13] K. Klier, *Adv. Catal.* **1982**, *31*, 243.
[14] H. Wilmer, M. Kurtz, K. V. Klementiev, O. P. Tkachenko, W. Grunert, O. Hinrichsen, A. Birkner, S. Rabe, K. Merz, M. Driess, C. Woll, M. Muhler, *Phys. Chem. Chem. Phys.* **2003**, *5*, 4736.
[15] S. Polarz, F. Neues, M. Van den Berg, W. Grünert, L. Khodeir, *J. Am. Chem. Soc.* **2005**, *127*, 12028.
[16] M. E. Franke, T. J. Koplin, U. Simon, *Small* **2006**, *2*, 36.
[17] G. Heiland, *Z. Phys.* **1954**, *138*, 459.
[18] G. Eranna, B. C. Joshi, D. P. Runthala, R. P. Gupta, *Crit. Rev. Solid State Mater. Sci.* **2004**, *29*, 111.
[19] N. Barsan, M. Schweizer-Berberich, W. Gopel, *Fresenius' J. Anal. Chem.* **1999**, *365*, 287.
[20] L. F. Dong, Z. L. Cui, Z. K. Zhang, *Nanostruct. Mater.* **1997**, *8*, 815.
[21] H. M. Lin, S. J. Tzeng, P. J. Hsiau, W. L. Tsai, *Nanostruct. Mater.* **1998**, *10*, 465.
[22] P. Mitra, A. P. Chatterjee, H. S. Maiti, *Mater. Lett.* **1998**, *35*, 33.
[23] B. Costello, R. J. Ewen, P. R. H. Jones, N. M. Ratcliffe, R. K. M. Wat, *Sens. Actuators, B* **1999**, *61*, 199.
[24] J. Q. Xu, Q. Y. Pan, Y. A. Shun, Z. Z. Tian, *Sens. Actuators, B* **2000**, *66*, 277.
[25] S. Roy, S. Basu, *Bull. Mater. Sci.* **2002**, *25*, 513.
[26] G. Sakai, N. Matsunaga, K. Shimanoe, N. Yamazoe, *Sens. Actuators, B* **2001**, *80*, 125.
[27] N. Matsunaga, G. Sakai, K. Shimanoe, N. Yamazoe, *Sens. Actuators, B* **2003**, *96*, 226.
[28] G. Korotcenkov, *Sens. Actuators, B* **2005**, *107*, 209.
[29] S. Polarz, J. Strunk, V. Ischenko, M. Van den Berg, O. Hinrichsen, M. Muhler, M. Driess, *Angew. Chem.* **2006**, *118*, 3031.
[30] S. Polarz, A. Orlov, M. Van den Berg, M. Driess, *Angew. Chem. Int. Ed.* **2005**, *44*, 7892.
[31] D. Schroeder, H. Schwarz, S. Polarz, M. Driess, *Phys. Chem. Chem. Phys.* **2005**, *7*, 1049.
[32] V. Ischenko, S. Polarz, D. Grote, V. Stavarache, K. Fink, M. Driess, *Adv. Funct. Mater.* **2005**, *15*, 1945.
[33] S. Polarz, A. Roy, M. Merz, S. Halm, D. Schröder, L. Scheider, G. Bacher, F. E. Kruis, M. Driess, *Small* **2005**, *1*, 540.
[34] A. Roy, S. Polarz, S. Rabe, B. Rellinghaus, H. Zahres, F. E. Kruis, M. Driess, *Chem. Eur. J.* **2004**, *10*, 1565.
[35] C. S. Rout, S. H. Krishna, S. R. C. Vivekchand, A. Govindaraj, C. N. R. Rao, *Chem. Phys. Lett.* **2006**, *418*, 586.
[36] J. Q. Xu, Y. P. Chen, Y. D. Li, J. N. Shen, *J. Mater. Sci.* **2005**, *40*, 2919.
[37] P. P. Sahay, S. Tewari, S. Jha, M. Shamsuddin, *J. Mater. Sci.* **2005**, *40*, 4791.
[38] P. Feng, Q. Wan, T. H. Wang, *Appl. Phys. Lett.* **2005**, 87.
[39] Q. Wan, Q. H. Li, Y. J. Chen, T. H. Wang, X. L. He, J. P. Li, C. L. Lin, *Appl. Phys. Lett.* **2004**, *84*, 3654.
[40] J. Q. Xu, Y. A. Shun, Q. Y. Pan, J. H. Qin, *Sens. Actuators, B* **2000**, *66*, 161.
[41] Y. Liu, E. Koep, M. Liu, *Chem. Mater.* **2005**, *17*, 3997.
[42] B. Meyer, *Phys. Rev. B: Condens. Matter Mater. Phys.* **2004**, *69*.
[43] D. Block, A. Herve, R. T. Cox, *Phys. Rev. B: Condens. Matter Mater. Phys.* **1982**, *25*, 6049.
[44] N. Y. Garces, L. Wang, L. Bai, N. C. Giles, L. E. Haliburton, G. Gantwell, *Appl. Phys. Lett.* **2002**, *81*, 622.
[45] J. Schneider, A. Rauber, *Z. Naturforsch.* **1961**, *16*, 712.
[46] H. Rose, *Optik* **1990**, *85*, 19.
[47] C. L. Jia, M. Lentzen, K. Urban, *Science* **2003**, *299*, 870.
[48] M. Haider, S. Uhlemann, E. Schwan, H. Rose, B. Kabius, K. Urban, *Nature* **1998**, *392*, 768.
[49] M. Lehmann, H. Lichte, *Cryst. Res. Technol.* **2005**, *40*, 149.
[50] M. K. Kennedy, F. E. Kruis, H. Fissan, B. R. Mehta, S. Stappert, G. Dumpich, *J. Appl. Phys.* **2003**, *93*, 551.
[51] M. K. Kennedy, F. E. Kruis, H. Fissan, B. R. Mehta, *Rev. Sci. Instrum.* **2003**, *74*, 4908.

FULL PAPERS

Chemical sensing on metal-oxide sensors is a complex phenomenon involving redox catalysis and electrical conductivity; effects like surface area, grain size, and, in addition, the occurrence of defects give separate contributions to the current. The importance of nontexture effects are compared to texture effects using ZnO as a model system (see figure). Highly sensitive and stable sensors are described.

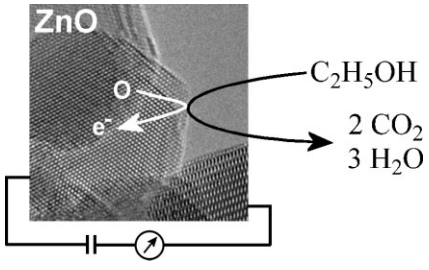

Sensors